

Nonparametric spectral density estimation from irregularly sampled data

Christopher J. Geoga*

Department of Statistics
University of Wisconsin-Madison
Madison, WI 53706

Paul G. Beckman[†]

Courant Institute
New York University
New York, NY 10012

Abstract

We introduce a nonparametric spectral density estimator for fully irregularly sampled points in one or more dimensions, constructed using a weighted nonuniform Fourier sum whose weights yield a high-accuracy quadrature rule for a user-specified window function. The resulting estimator significantly reduces the aliasing seen in periodogram approaches and least squares spectral analysis, sidesteps the dangers of ill-conditioning of the nonuniform Fourier inverse problem, and can be adapted to a wide variety of irregular sampling settings. After a discussion of methods for computing the necessary weights and a theoretical analysis of sources of bias, we close with demonstrations of the method's efficacy, including for processes that exhibit very slow spectral decay and for processes in multiple dimensions.

Keywords: spectral density, nonparametrics, nonuniform fast Fourier transform, quadrature

*corresponding author: geoga@wisc.edu

[†]PGB is supported in part by the Office of Naval Research under award #N00014-21-1-2383 and by the U.S. Department of Energy, Office of Science, Office of Advanced Scientific Computing Research, Department of Energy Computational Science Graduate Fellowship under Award Number DE-SC0022158

1 Introduction

Let $Y(\mathbf{x})$ be a stochastic process indexed by $\mathbf{x} \in \mathbb{R}^d$ with finite second moments. Consider the case of a *weakly stationary* $Y(\mathbf{x})$ with $\mathbb{E}Y(\mathbf{x}) \equiv 0$, so that its covariance function $K(\mathbf{x}, \mathbf{x}') := \text{Cov}(Y(\mathbf{x}), Y(\mathbf{x}'))$ is shift-invariant, meaning $K(\mathbf{x}, \mathbf{x}') = K(\mathbf{x} + \mathbf{h}, \mathbf{x}' + \mathbf{h})$ for all $\mathbf{h} \in \mathbb{R}^d$. In this setting, we may study the covariance function in a single-argument form as $K(\mathbf{x} - \mathbf{x}') = \text{Cov}(Y(\mathbf{x}), Y(\mathbf{x}'))$. By the Wiener-Khinchin theorem [24], if K is real-valued and continuous, then there exists a function $S(\boldsymbol{\omega})$ that is non-negative, integrable, and symmetric about the origin (so that $S(\boldsymbol{\omega}) = S(-\boldsymbol{\omega})$) such that

$$K(\mathbf{x} - \mathbf{x}') = \int_{\mathbb{R}^d} e^{2\pi i \boldsymbol{\omega}^T (\mathbf{x} - \mathbf{x}')} S(\boldsymbol{\omega}) \, d\boldsymbol{\omega}.$$

This function $S(\boldsymbol{\omega})$ is called the *spectral density*, and features of $S(\boldsymbol{\omega})$ such as integrable singularities or finite moments $\int_{\mathbb{R}^d} \|\boldsymbol{\omega}\|_2^{2s} S(\boldsymbol{\omega}) \, d\boldsymbol{\omega} < \infty$ have precise implications regarding sample-path properties of $Y(\mathbf{x})$. For these reasons, a large amount of the theory for problems like prediction, interpolation, and estimation in time series analysis and Gaussian processes is expressed in the *spectral* domain. We refer the reader to [6, 43] for further discussion.

Considering the interpretive value of $S(\boldsymbol{\omega})$ and the computational efficiency of the fast Fourier transform (FFT), the task of obtaining nonparametric estimators for $S(\boldsymbol{\omega})$ is a large area of research. Tools for this problem are particularly mature for gridded data in one dimension, where a wide variety of methods for specific applications have been developed and provide excellent results (see [45, 36, 35, 31, 34] and references therein). To reduce finite-sample sources of bias for data being modeled as truly discrete-time, many nonparametric estimators in this setting make use of a *window function*, which we will denote $g(x)$ and for the moment will assume is defined on $[0, 1]$ with unit norm $\|g\|_{L^2([0,1])} = 1$ and Fourier transform $G(\omega) = \int_0^1 e^{-2\pi i \omega x} g(x) \, dx$. For gridded one-dimensional data sampled on $\{0, 1, \dots, n-1\}$, one can estimate the spectral density $S : [-\frac{1}{2}, \frac{1}{2}] \rightarrow [0, \infty)$ at frequency k/n for $-n/2 \leq k < n/2$ as

$$\hat{S}(k/n) = \left| \frac{1}{\|g\|_2} \sum_{j=0}^{n-1} e^{-2\pi i k j/n} g_j y_j \right|^2, \quad (1.1)$$

where $\mathbf{g} := [g(j/n)]_{j=0}^{n-1}$ is the vector generated by the window function $g(x)$. A standard computation shows that in this setting we have

$$\mathbb{E}\hat{S}(k/n) = \int_{-1/2}^{1/2} |G_n(k/n - \omega)|^2 S(\omega) \, d\omega = (|G_n|^2 * S)(k/n) \quad (1.2)$$

where $G_n(\omega) := \frac{1}{\|g\|_2} \sum_{j=0}^{n-1} e^{-2\pi i j \omega} g_j$. Naturally, the ideal window function $g(x)$ would be one that corresponds to $|G_n(\omega)|^2 \approx \delta(\omega)$, so that $\hat{S}(k/n)$ would be an unbiased estimator of $S(k/n)$. For finite n , the Heisenberg uncertainty principle enforces an upper bound on how closely $|G_n(\omega)|^2$ can possibly approximate the idealized, perfectly concentrated delta function [40, 17]. Nevertheless, designing window functions with favorable concentration properties remains a driving motivation and important practical concern. The choice $g_j \equiv 1$ implicitly corresponds

to selecting the window $g(x) = \mathbf{1}_{\{x \in [0,1]\}}$, in which case the estimator (1.1) is referred to as the *periodogram* [6]. In this case one obtains

$$n^{-\frac{1}{2}}G_n(k/n) = \frac{1}{n} \sum_{j=0}^{n-1} e^{-2\pi i k j/n} \approx \int_0^1 e^{-2\pi i k x} dx = e^{-ik\pi} \text{sinc}(\pi k) = G(k). \quad (1.3)$$

The approximate equality above is due to interpreting the summation as an approximation to the continuous integral using the trapezoidal rule. For integrands that are smooth and periodic, the trapezoidal rule converges exponentially [49] and the above approximation is very accurate. While this is not the typical perspective taken in analyzing window functions, this quadrature view will form the basis of the new methods proposed in this work.

In the case of irregular sampling, where $\{x_j\}_{j=1}^n$ is not a subset of some Cartesian grid, the spectral estimation problem becomes much more challenging. The first complication is that one typically treats such measurements as coming from a continuous-time (or continuous space-time) process. Unlike the case of truly discrete time series at regular sampling intervals, in which the spectral density can be represented on the finite interval $[-\frac{1}{2}, \frac{1}{2}]$, for continuous-time models $S(\omega)$ is supported on \mathbb{R} (or \mathbb{R}^d for multi-dimensional processes). By information-theoretic limits like the Shannon-Nyquist sampling theorem [38, 28], the spectral density $S(\omega)$ may be supported on frequency bands that are unresolvable from observations at the given locations $\{x_j\}_{j=1}^n$.

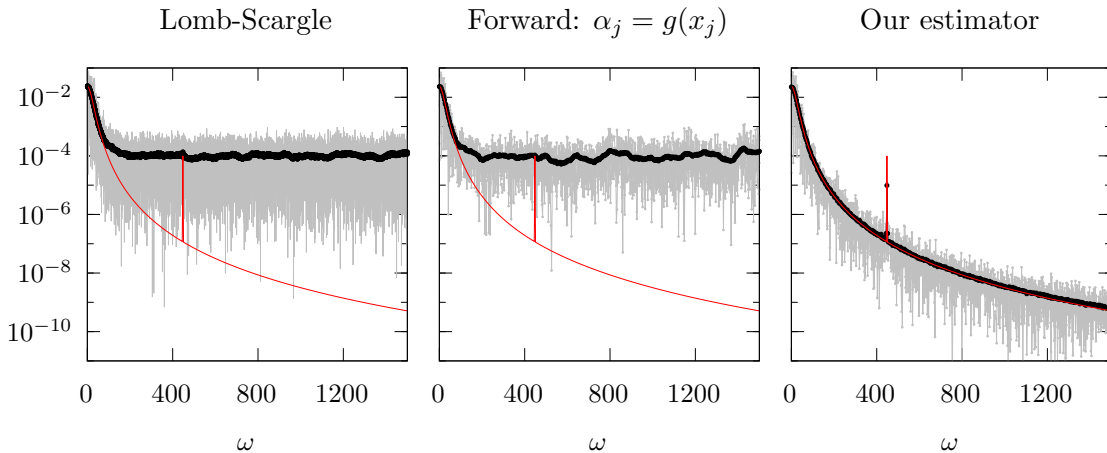


Figure 1: A comparison of two existing estimators with the estimator proposed in this work, applied to the problem of estimating the spectral density $S(\omega)$ of a process $Y(x)$ on $[0, 1]$ with Matérn covariance and a faint spectral line measured at $n = 10,000$ locations sampled uniformly on $[0, 1]$. Individual estimates for many samples are shown in grey, their average is shown in black, and the true SDF $S(\omega)$ is shown in red. The forward estimator is as defined in (1.4).

A number of approaches have been proposed for estimating spectral densities for continuous-time processes from irregular data, including maximum likelihood [44] and multiband methods [7, 9]. One particularly popular approach is to adopt a least squares standpoint, fitting a sinusoidal model to the data at a single frequency ω and using the fitted coefficients to estimate $S(\omega)$. This is the approach taken by the *Lomb-Scargle* periodogram [29, 37, 51],

which is a popular and successful tool for processes $Y(x)$ which have strong purely periodic components or *spectral lines*. Many other algorithms for identifying and estimating discrete periodic components have been proposed, and we refer readers to [3] and references therein for a review. However, because these methods estimate $S(\omega)$ at a single frequency or a small collection of discrete frequencies at a time, they are not well-suited to recovering continuous spectral densities, in which case these estimates may be highly biased by aliasing or *spectral leakage* from other frequencies. The left panel in Figure 1 shows an example of the Lomb-Scargle periodogram being used to estimate a continuous spectral density and suffering from aliasing error.

An alternative approach is to reweight an estimator of the form (1.1) to more effectively control the aliasing error for irregular sampling locations. Assume now that we observe a process $Y(x)$ at irregular points $\{x_j\}_{j=1}^n \subset [a, b]$. Let $\boldsymbol{\alpha} = [\alpha_j]_{j=1}^n \in \mathbb{C}^n$ be weights corresponding to the observation locations. A weighted “forward” estimator is then given by

$$\hat{S}(\xi) = \left| \sum_{j=1}^n e^{-2\pi i \xi x_j} \alpha_j y_j \right|^2. \quad (1.4)$$

Estimators of this form are computationally appealing, as the nonuniform Fourier sum can be evaluated at m frequencies $\{\xi_k\}_{k=1}^m$ in $\mathcal{O}(n + m \log m)$ time using the nonuniform fast Fourier transform (NUFFT) [11, 4]. The variance computations performed above can still be done here, and we see again from an application of the Wiener-Khinchin theorem that

$$\mathbb{E} \hat{S}(\xi) = \int_{\mathbb{R}} |H_{\boldsymbol{\alpha}}(\xi - \omega)|^2 S(\omega) d\omega = (|H_{\boldsymbol{\alpha}}|^2 * S)(\xi) \quad (1.5)$$

where $H_{\boldsymbol{\alpha}}(\omega) := \sum_{j=1}^n e^{-2\pi i \omega x_j} \alpha_j$. One straightforward choice of weights is to take $\alpha_j = g(x_j)$ [33] (see also [42] for a combination of this window design approach with the Lomb-Scargle periodogram). However, unlike in the equispaced case (1.3) in which the trapezoidal rule yields an accurate approximation to the relevant integral, there is no reason to expect that $H_{\boldsymbol{\alpha}}(\omega) \approx \int_a^b e^{-2\pi i \omega x} g(x) dx$ in this case, as $\{g(x_j)\}_{j=1}^n$ do not constitute quadrature weights for the irregular nodes $\{x_j\}_{j=1}^n$. Therefore, even with a choice of $g(x)$ that has small bias in the gridded case with $|G_n(\omega)|^2 \approx \delta(\omega)$, this choice of weights leads to estimators which suffer from the same aliasing as the un-windowed periodogram on irregular data, as noted in [42]. In the case of gappy gridded data, it is possible to repair the weights and achieve good estimator properties in a reasonably simple way [8, 10], but these methods do not translate to fully unstructured irregular sampling regimes. The middle panel of Figure 1 shows a typical example in which, despite choosing a window $g(x)$ such that $G(\omega)$ is highly concentrated, the estimator suffers from large biases when one simply chooses $\alpha_j = g(x_j)$.

In this work, we propose and analyze an estimator of the form (1.4) where the weights $\boldsymbol{\alpha}$ are designed to satisfy the requirement that

$$H_{\boldsymbol{\alpha}}(\omega) = \sum_{j=1}^n e^{-2\pi i \omega x_j} \alpha_j \approx \int_a^b e^{-2\pi i \omega x} g(x) dx = G(\omega) \quad (1.6)$$

for all $|\omega| \leq \Omega$, a frequency cutoff that will be discussed extensively in this work and can be considered a continuous analog to the Nyquist frequency. Choosing weights $\boldsymbol{\alpha}$ in this way

restores the intuition that $|H_{\alpha}(\omega)|^2 \approx \delta(\omega)$ —in particular, that the weighted *spectral window* is well concentrated—which we observed in the equispaced case (1.3). In addition, this choice to approximate a smooth, concentrated function $G(\omega)$ with sinusoids rather than directly solving least squares problems involving non-smooth, non-concentrated data \mathbf{y} significantly reduces bias and permits a more concrete analysis using tools from nonuniform sampling, interpolation, and quadrature. Our estimator is shown alongside two existing methods discussed above in Figure 1, providing a dramatic example of potential improvements our proposed method offers for fully irregularly measured data.

In the next section, we discuss the existence and computation of the weights α that make our estimator possible. Following that, we provide some theory for understanding the performance of the estimator, both of which are materially more subtle than in the standard gridded case. Finally, we close with a variety of demonstrations, including numerical validations of the theory given in this work and a demonstration of our estimator on two-dimensional, fully irregular data.

2 A new spectral density estimator

For expositional clarity, we develop the method here in one dimension. Where relevant, we provide comments on technical differences in multidimensional settings, but otherwise the translation of these tools and algorithms to higher dimensions is direct.

Let $\mathbf{y} = [Y(x_j)]_{j=1}^n$ denote measurements of the process $Y(x)$ at potentially non-equidistant locations $\{x_j\}_{j=1}^n$. As discussed above, we propose to compute estimators of the form (1.4) where the weights $\alpha \in \mathbb{C}^n$ are designed specifically to satisfy (1.6) for all $|\omega| \leq \Omega$. Given such weights α , we can decompose the expectation of our estimator as

$$\begin{aligned} \mathbb{E}\hat{S}(\xi) &= \int_{\mathbb{R}} |H_{\alpha}(\xi - \omega)|^2 S(\omega) d\omega \\ &\approx S(\xi) + \underbrace{\int_{\xi-W}^{\xi+W} |G(\xi - \omega)|^2 S(\omega) d\omega}_{\text{window-induced bias}} - S(\xi) \\ &\quad + \underbrace{\int_{-\infty}^{\xi-\Omega} |H_{\alpha}(\xi - \omega)|^2 S(\omega) d\omega}_{\text{lower aliasing bias}} + \underbrace{\int_{\xi+\Omega}^{\infty} |H_{\alpha}(\xi - \omega)|^2 S(\omega) d\omega}_{\text{upper aliasing bias}}. \end{aligned} \tag{2.1}$$

The domain in the second term above is reduced because, by assumption on $G(\omega)$, the contribution in the intervals $[-\Omega, -W]$ and $[W, \Omega]$ can be made exceptionally small, for example

$$\int_{[-\Omega, -W] \cup [W, \Omega]} |G(\xi - \omega)|^2 S(\omega) d\omega < 10^{-16}$$

for $W \ll \Omega$. If S does not vary wildly on the narrow interval $[\xi - W, \xi + W]$, then the second term will also be small. This leaves only the lower and upper aliasing terms—which are by far the dominant sources of bias—to be analyzed. With (1.6) and (2.1) in mind, there are three main design considerations which must be addressed in order to compute suitable weights α :

1. selecting the maximum controlled frequency Ω and computing the weights α so that $H_\alpha(\omega) \approx G(\omega)$ for all $|\omega| \leq \Omega$,
2. choosing the window $g(x)$ so that $G(\omega)$ is maximally concentrated in order to minimize the window-induced bias, and
3. balancing the fundamental tradeoff between increasing Ω , which permits the estimation of $S(\xi)$ at higher frequencies, and minimizing $\|\alpha\|_2$, which has a direct relationship with the magnitude of the aliasing biases.

In the following three sections we treat each of these considerations in turn, establishing a theoretical basis for the accuracy and limitations of our estimator.

2.1 Computing the weights

For the moment, let us assume that the window function $g(x)$ is given. We will return to the problem of selecting $g(x)$ in Section 2.2. The problem of computing weights α which satisfy (1.6) is precisely the problem of designing a *quadrature rule* with fixed node locations $\{x_j\}_{j=1}^n$ which accurately integrates the family of functions $\{x \mapsto e^{-2\pi i\omega x}\}_{\omega \in [-\Omega, \Omega]}$ under the weight function $g(x)$. If the nodes $\{x_j\}_{j=1}^n$ can be chosen freely, then one could compute a *Gaussian quadrature rule* which integrates these functions to high accuracy [13, 55, 47, 27]. A particularly simple choice would be to choose $\{x_j\}_{j=1}^n$ to be the zeros of the n -th order Legendre polynomial, in which case *Gauss-Legendre* quadrature weights $\{\gamma_j\}_{j=1}^n$ can be computed and $\alpha = \{\gamma_j g(x_j)\}_{j=1}^n$ will satisfy (1.6). These nodes and weights can be computed very rapidly and accurately even for large n [12, 20], and so for practitioners who have the freedom to choose design points, this course of action provides an immediate and straightforward choice of weights.

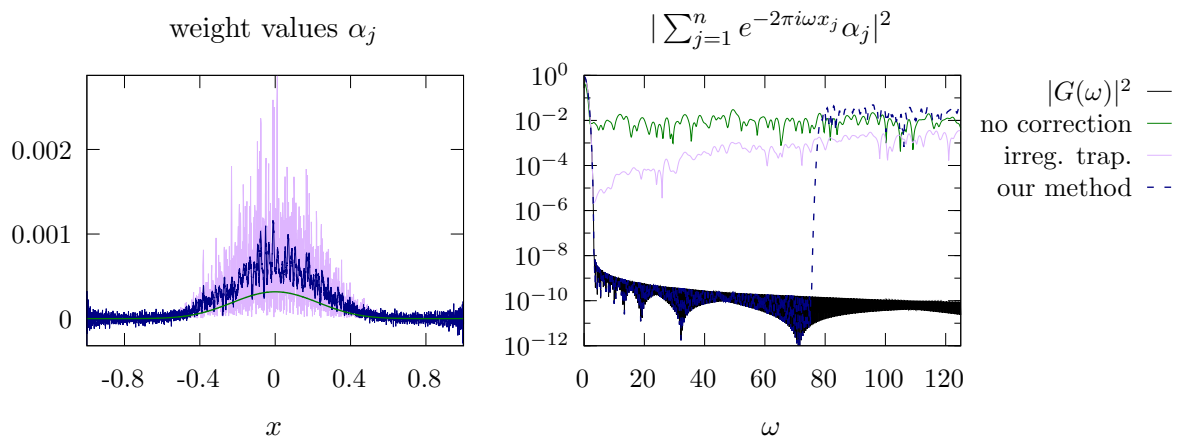


Figure 2: Accuracy of various weighting schemes in recovering $G(\omega)$ using a weighted Fourier sum with arbitrary locations $\{x_j\} \subset [-1, 1]$. Weights for our method are computed with $\Omega = 75$. The window $g(x)$ is chosen to be a Kaiser function, discussed in the next sub-section, and the weights in a unified notation are $\alpha_j = g(x_j)/n$ for no correction and $\alpha_j = g(x_j)\gamma_j$ as in (2.2) for the irregular trapezoidal scheme.

In the much more common case in which data are provided at arbitrary irregular locations $\{x_j\}_{j=1}^n$ without input from the analyzing statistician, no such high-order quadrature exists a priori. One particularly simple choice of low-order quadrature rule in this setting is an irregular trapezoidal rule with weights

$$\gamma_j = \begin{cases} (x_2 - x_1)/2 & \text{for } j = 1 \\ (x_{j+1} - x_{j-1})/2 & \text{for } 1 < j < n \\ (x_n - x_{n-1})/2 & \text{for } j = n. \end{cases} \quad (2.2)$$

These weights are sometimes referred to as *density compensation factors* in imaging inverse problems [16, 52, 1], and may be satisfactory for estimating spectral densities at low to moderate frequencies from densely-sampled or quasi-equispaced data. However, as is demonstrated in Figure 2, even mild gaps in the data lead to large errors when integrating sufficiently oscillatory functions.

In order to develop an alternative quadrature rule on irregular nodes $\{x_j\}_{j=1}^n$ which gives higher accuracy, we turn (1.6) into a linear system which can be solved for the weights α . For this purpose, we take $\omega_k := \Omega \cos(\frac{2k-1}{2n}\pi)$ for $k = 1, \dots, n$ to be Chebyshev nodes on $[-\Omega, \Omega]$. Let $\mathcal{F} \in \mathbb{C}^{n \times n}$ denote the nonuniform discrete Fourier matrix given by $\mathcal{F}_{jk} := e^{-2\pi i \omega_j x_k}$ and define $\mathbf{b} := [G(\omega_j)]_{j=1}^n$. Then we seek solutions α to the linear system

$$\mathcal{F}\alpha = \mathbf{b}. \quad (2.3)$$

The matrix \mathcal{F} is exceptionally ill-conditioned in most cases [32]. However, by using the fact that $G(\omega)$ is entire, the following theorem demonstrates that with mild oversampling, a high-quality solution α to the linear system (2.3)—and thus a suitable choice of weights satisfying (1.6)—is guaranteed to exist.

Theorem 1. *Take $\Omega > 0$ and $a \leq x_1 < \dots < x_n \leq b$. Let G be bandlimited with $\text{supp}(g) \subseteq [a, b]$. Then for any $\rho > 1$ there exist weights $\alpha \in \mathbb{C}^n$ such that*

$$\|H_\alpha - G\|_{L^\infty([-\Omega, \Omega])} \leq \frac{4}{\rho - 1} \exp \left\{ \frac{\pi}{2} \Omega (b - a) (\rho + \rho^{-1}) - n \log \rho \right\} \left(\|g\|_{L^1([a, b])} + \|\alpha\|_1 \right).$$

Proof. Let $\{\omega_k\}_{k=1}^n$ be Chebyshev nodes on $[-\Omega, \Omega]$. Then the linear system

$$H_\alpha(\omega_k) = \sum_{j=1}^n \alpha_j e^{-2\pi i \omega_k x_j} = G(\omega_k), \quad k = 1, \dots, n \quad (2.4)$$

has a unique solution $\alpha \in \mathbb{C}^n$ for which the order- n Chebyshev interpolants of G and the resulting H_α are everywhere equal. H_α and G are band-limited and can thus be analytically extended to entire functions, and therefore their pointwise error converges to zero exponentially as

$$\|H_\alpha - G\|_{L^\infty([-\Omega, \Omega])} \leq \frac{4M(\rho)\rho^{-n}}{\rho - 1} \quad (2.5)$$

for all $\rho > 1$, where $|H_\alpha(z) - G(z)| \leq M(\rho)$ for all $z \in E_\rho$ and $E_\rho := \{(z + z^{-1})/2 : |z| = \rho\}$ is the ρ -Bernstein ellipse [47, Theorem 8.2]. Defining $F(z) := H_\alpha(z) - G(z)$, we can compute

the explicit bound

$$\begin{aligned}
|F(z)| &= |F(p + iq)| \\
&= \left| \int_{-\frac{\Omega}{2}(b-a)}^{\frac{\Omega}{2}(b-a)} \left(\sum_{j=1}^n \alpha_j \delta(x - x_j) - g(x) \right) e^{-2\pi i(p+iq)x} dx \right| \\
&\leq \int_{-\frac{\Omega}{2}(b-a)}^{\frac{\Omega}{2}(b-a)} \left(\sum_{j=1}^n |\alpha_j| \delta(x - x_j) + |g(x)| \right) e^{2\pi q x} dx \\
&\leq e^{\pi\Omega(b-a)|z|} \left(\|g\|_{L^1([a,b])} + \|\boldsymbol{\alpha}\|_1 \right)
\end{aligned}$$

The point in E_ρ with largest magnitude is $z = \frac{\rho + \rho^{-1}}{2}$. Thus we have

$$|F(z)| \leq \exp \left\{ \frac{\pi}{2} \Omega (b-a) (\rho + \rho^{-1}) \right\} \left(\|g\|_{L^1([a,b])} + \|\boldsymbol{\alpha}\|_1 \right) =: M(\rho)$$

for all $z \in E_\rho$. The result then follows from (2.5). \square

Note that we can choose the rate of decay ρ in Theorem 1 to be arbitrarily large, at the cost of an increased multiplicative constant $M(\rho)$. Therefore, this theorem demonstrates that the approximation error between $H_\alpha(\omega)$ and $G(\omega)$ on the interval $\omega \in [-\Omega, \Omega]$ decays *superexponentially* in n (i.e. faster than any exponential), with a rate and prefactor which depend on the space-frequency product $2\Omega(b-a)$ and the choice of ρ .

To make this result more concrete, we provide the following corollary, which fixes ρ and studies the oversampling necessary to achieve double precision relative accuracy in the recovery problem.

Corollary 1. *Take $\varepsilon > 10^{-16}$ and assume $\|g\|_{L^1([a,b])} \leq \|\boldsymbol{\alpha}\|_1$. Then under the assumptions of Theorem 1, for any n such that*

$$n \geq 4.8 \cdot \Omega(b-a) + 35,$$

there exist weights $\boldsymbol{\alpha} \in \mathbb{C}^n$ such that

$$\|H_\alpha - G\|_{L^\infty([-\Omega, \Omega])} \leq \varepsilon \|\boldsymbol{\alpha}\|_1$$

Proof. Take $\rho = 3$ in Theorem 1, set the right hand side equal to $2\varepsilon \|\boldsymbol{\alpha}\|_1$, and use the facts $\frac{5\pi}{3 \log 3} < 4.8$ and $-\log_3 \left(\frac{10^{-16}}{4} \right) < 35$. \square

As the Nyquist frequency in this setting is $\Omega_{\text{nyq}} := \frac{n}{4(b-a)}$, Corollary 1 roughly states that the window recovery problem can be solved to 16 digits of relative accuracy for any $\Omega \leq 0.8\Omega_{\text{nyq}}$. However, as we will see in Section 2.2, this may result in prohibitively large oscillatory weights depending on the choice of $g(x)$.

It is worth emphasizing that the window reconstruction problem differs in several important ways from the well-studied *irregular sampling* problem of computing Fourier coefficients from data by solving the inverse problem $\mathcal{F}^* \mathbf{c} = \mathbf{y}$ [5, 2, 1, 16]. Computing weights $\boldsymbol{\alpha}$ which satisfy $\mathcal{F}\boldsymbol{\alpha} = \mathbf{b}$ when $G(\omega)$ is a smooth, bandlimited, concentrated function is possible even

when the general inverse problem is hopelessly ill-conditioned, and no such weights could be stably computed for non-smooth, noisy data. In the irregular sampling problem $\mathcal{F}^* \mathbf{c} = \mathbf{y}$, clustered points x_j induce ill-conditioning as small perturbations to the samples y_j can lead to wild oscillations in the recovered coefficients \mathbf{c} . However, in our window reconstruction setting, the existence of $\boldsymbol{\alpha}$ requires only that the window function $G(\omega)$ lies approximately in $\text{span}(\{e^{-2\pi i \omega x_j}\}_{j=1}^n)$ for $\omega \in [-\Omega, \Omega]$, from which one can compute accurate weights $\boldsymbol{\alpha}$ using any backwards stable method of solving the least squares problem $\mathcal{F}\boldsymbol{\alpha} = \mathbf{b}$, for example a Householder QR factorization [48]. Therefore adding sampling points x_j can only improve the accuracy of the reconstructed window $H_{\boldsymbol{\alpha}}(\omega)$.

Computing $\boldsymbol{\alpha}$ by solving the dense linear system $\mathcal{F}\boldsymbol{\alpha} = \mathbf{b}$ requires $\mathcal{O}(n^3)$ operations if $\Omega = \mathcal{O}(n)$. For fixed $\Omega = \mathcal{O}(1)$, however, the rank of \mathcal{F} will stay roughly constant as n grows and so using an early-terminating factorization (for example rank-revealing [19] or randomized [22] methods) will require only $\mathcal{O}(n)$ operations. While we do not pursue the question of accelerating computations in the $\Omega = \mathcal{O}(n)$ case here, there are several promising avenues for potentially doing so [25, 26, 53].

2.2 Choosing a window

We now turn to the problem of designing a suitable window function $g(x)$. As has been discussed already, the primary quality that a window must have is that its Fourier transform $G(\omega) = \int_a^b g(x)e^{-2\pi i \omega x} dx$ is as close to zero as possible outside of a user-controlled ball of radius W at the origin. Assuming momentarily that $g(x)$ is supported on $[-1/2, 1/2]$ for notational convenience and normalized so that $\|g\|_{L^2([0,1])} = 1$, the *spectral concentration* of $g(x)$ on $[-W, W]$ is given by

$$\lambda(g) := \int_{-W}^W |G(\omega)|^2 d\omega. \quad (2.6)$$

We note that $\lambda(g) < 1$, and the closer this concentration is to one the closer $g(x)$ is to being a truly bandlimited function (which is not possible for any function with finite support). In [41], the authors prove that the *optimally* concentrated function in the sense of maximizing λ is the dominant eigenfunction of the linear integral operator

$$T_A : f(x) \mapsto \int_{-1/2}^{1/2} \text{sinc}(W(t-x))f(t) dt,$$

and [39] gives a more general convenient form of this operator in multiple dimensions for functions $f(\mathbf{x})$ defined on domains \mathcal{D} and with arbitrary regions of concentration \mathcal{R} given by

$$T_A : f(\mathbf{x}) \mapsto \int_{\mathcal{D}} \left\{ \int_{\mathcal{R}} e^{2\pi i \mathbf{s}^T (\mathbf{t}-\mathbf{x})} d\mathbf{s} \right\} f(\mathbf{t}) d\mathbf{t}. \quad (2.7)$$

Such optimally concentrated functions are called *prolate spheroidal wavefunctions* (PSWFs), and informally referred to as prolate functions. Many fast and accurate numerical methods and algorithms for evaluating prolate functions exist [54, 18, 15]. We provide a brief discussion in Appendix A and implement relevant routines in the software companion to this work¹.

¹A polished software companion suite to this work, complete with documentation, is under development.

As a simple option for data observed on an interval in one dimension, an approximation to the prolate is given in closed form by the *Kaiser* window [23]. For $[a, b] = [-\frac{1}{2}, \frac{1}{2}]$, this window is given in the time and Fourier domain by

$$g(x) = \mathbf{1}_{\{x \in [-1/2, 1/2]\}} c_0 I_0(\beta \sqrt{2x}) \quad G(\omega) = \begin{cases} \frac{c_0 \sinh(\sqrt{\beta^2 - (2\pi\omega)^2})}{\sqrt{\beta^2 - (2\pi\omega)^2}} & |2\pi\omega| < \beta \\ c_0 \operatorname{sinc}(\sqrt{(2\pi\omega)^2 - \beta^2}) & |2\pi\omega| \geq \beta \end{cases}, \quad (2.8)$$

where I_0 is the first-kind modified Bessel function, β is a shape parameter, and c_0 is selected so that $\|g\|_{L^2([-\frac{1}{2}, \frac{1}{2}])} = 1$ [30]. It is straightforward to shift and rescale this Fourier transform pair so that $g(x)$ is supported on an arbitrary interval $[a, b]$, and we will not comment in detail on such transformations when they are done. While the prolate function is the theoretically superior choice, the Kaiser window is fast and convenient to evaluate and gives comparable performance in practice, and thus we utilize it in a number of numerical demonstrations here.

For the purposes of our estimator, it is also important that the window function $g(x)$ is smooth and only supported on domains containing the sampling locations. The motivation for these soft requirements is more subtle than the first and pertains to controlling the norm of $\boldsymbol{\alpha}$. As Theorem 1 indicates, if $\|\boldsymbol{\alpha}\|_1$ is large, then the absolute error $\|H_{\boldsymbol{\alpha}} - G\|_{L^\infty([a, b])}$ in the window reconstruction will in general also be large. In addition, we will see in Section 2.3 that $\|\boldsymbol{\alpha}\|_2$ controls the size of the aliasing biases.

In order to provide a heuristic argument that the smoothness and support of $g(x)$ are imperative to controlling $\|\boldsymbol{\alpha}\|_2$ in practice, we return to the linear system $\mathcal{F}\boldsymbol{\alpha} = \mathbf{b}$. Consider taking an SVD to obtain $\mathbf{U}\mathbf{D}\mathbf{V}^* = \mathcal{F}$, where $\mathbf{U}, \mathbf{V} \in \mathbb{C}^{n \times n}$ are unitary matrices, and $\mathbf{D} \in \mathbb{R}^{n \times n}$ is a diagonal matrix whose entries are the singular values $\{\sigma_j\}_{j=1}^n$ of \mathcal{F} . Since the ℓ_2 norm is invariant to unitary transformations, we have $\|\boldsymbol{\alpha}\|_2 = \|\mathbf{D}^{-1}\mathbf{U}^*\mathbf{b}\|_2$. As previously noted, the nonuniform Fourier matrix \mathcal{F} is typically highly ill-conditioned, and thus its singular values decay rapidly. If \mathbf{b} lies approximately in the span of the dominant r eigenvectors of \mathcal{F} , then $(\mathbf{U}^*\mathbf{b})_j \approx 0$ for $j > r$, and thus $(\mathbf{U}^*\mathbf{b})_j/\sigma_j$ remains small in magnitude even for very small singular values σ_j . In contrast, if \mathbf{b} is not orthogonal to the singular vectors corresponding to small singular values σ_j , then $(\mathbf{U}^*\mathbf{b})_j/\sigma_j \gg 1$ for some j , and $\|\boldsymbol{\alpha}\|_2$ will also be large. If $g(x)$ is large in some interval where no sampling locations lie, then we are attempting to approximate $G(\omega)$ by sinusoids whose dominant column space does not include the relevant frequencies. Similarly, if $g(x)$ contains discontinuities in its derivatives, then $G(\omega)$ will decay slowly, and more sinusoids are necessary to capture its behavior on its larger domain of numerical support. For a smooth $g(x)$ which takes large values only in regions where sampling locations are present, we avoid these numerical issues, so that $G(\omega)$ and the corresponding \mathbf{b} lie handily in the span of the dominant eigenvectors and $\|\boldsymbol{\alpha}\|_2$ is small. We discuss potential avenues for making this intuition rigorous and automating the selection of $G(\omega)$ in Section 4.

Figure 3 provides a visual demonstration of this phenomenon. Data locations are chosen to be uniformly distributed on $[-1, 1] \setminus [-0.15, 0]$, meaning that there will necessarily be a gap in the sorted points of size at least 0.15. While the recovered weights $\boldsymbol{\alpha}$ for window $g(x)$ selected to be a standard Kaiser window on $[-1, 1]$ do still provide a reasonably well-concentrated approximation $H_{\boldsymbol{\alpha}}(\omega)$ (accounting for the loss of a few digits due to the size of $\|\boldsymbol{\alpha}\|_2$), the weights have a norm on the order of 10^{11} . Using a prolate that has been adapted specifically

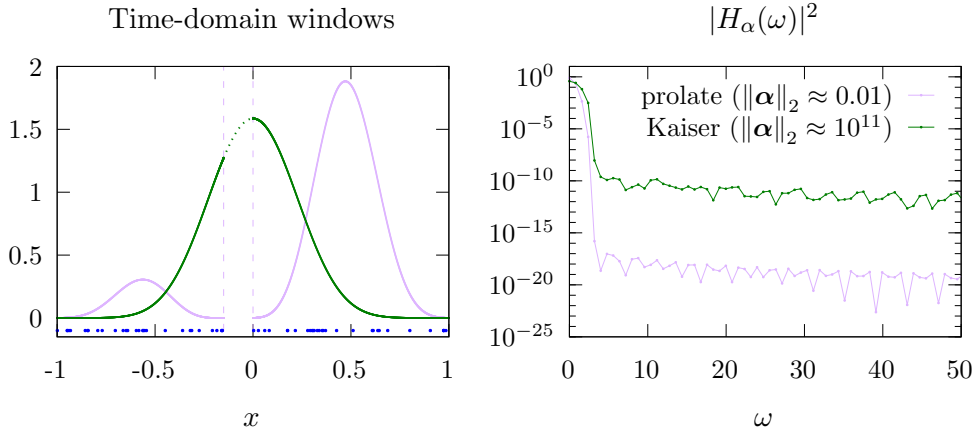


Figure 3: A comparison of the recovered window $|H_\alpha(\omega)|^2$ in a sampling setting with uniform points on $[-1, 1] \setminus [-0.15, 0]$ using a generic Kaiser window supported on $[-1, 1]$ and a prolate window supported on the precise domain.

to the data domain $\mathcal{D} = [-1, 1] \setminus [-0.15, 0]$, on the other hand, provides weights with a norm 13 orders of magnitude smaller and concentration at the level of machine precision.

2.3 Controlling aliasing bias

With the discussion of properly computing the weights α complete, we now turn to an analysis of the aliasing-based sources of bias in the estimator $\hat{S}(\xi)$. For the duration of this section, we will assume the following:

- (A1) Measurement locations $\{x_j\}_{j=1}^n$ are i.i.d. samples from a probability density function $p(x)$.
- (A2) The sampling density $p(x)$ is symmetric about the origin and supported on $[-a, a]$, so that its corresponding characteristic function $\varphi(t) = \mathbb{E}_{X \sim p} e^{2\pi i t X}$ is real-valued.
- (A3) The weights α have been computed to sufficient accuracy that we may treat $H_\alpha(\omega) \approx G(\omega)$ as an equality for $|\omega| < \Omega$.
- (A4) The maximum resolvable frequency Ω for weights α is large enough that $\varphi(2\Omega) \gg \varphi(\Omega)^2$, and we may treat $\varphi(2\Omega) - \varphi(\Omega)^2 \approx \varphi(2\Omega)$ as an equality.
- (A5) Ω may grow with n , but only at a rate such that there exist weights α with $\|\alpha\|_1 = \mathcal{O}(1)$. Consequently, the dependence of Ω and α on n will be suppressed.

We note that (A2) and (A4) are for notational simplicity and can be removed with no impact on the results beyond additional notation. The assumption (A5) is milder than it seems, and simply rules out edge cases in which Ω asymptotically converges to the Nyquist frequency in a way that induces the weights α to become oscillatory and grow in norm. As a reminder, by construction one has that $\sum_{j=1}^n \alpha_j \approx G_0 := G(0)$, and so if $\{\alpha_j\}_{j=1}^n$ is not overly oscillatory then $\|\alpha\|_1 \approx G_0$ and this condition will naturally be satisfied.

Under these assumptions, we now study the two aliasing error-based bias terms shown in (2.1). Writing the estimator as $\hat{S}(\xi_j) = |\eta_j|^2$ with $\boldsymbol{\eta} = \mathcal{F} \cdot \text{Diag}(\boldsymbol{\alpha}) \cdot \mathbf{y}$ and letting $\hat{\mathbf{s}} = [\hat{S}(\xi_j)]_{j=1}^n$ denote the vector of estimators we have that

$$\mathbb{E}\hat{\mathbf{s}} = \text{Diag}(\mathbf{M}) := \text{Diag}\left(\mathcal{F}\text{Diag}(\boldsymbol{\alpha})\boldsymbol{\Sigma}\text{Diag}(\boldsymbol{\alpha})\mathcal{F}^*\right),$$

where $\mathbf{y} = [Y(x_j)]_{j=1}^n$ and $\boldsymbol{\Sigma} = \mathbb{E}\mathbf{y}\mathbf{y}^T$ is its covariance matrix. Therefore, by (2.1) we have that

$$\varepsilon(\xi_j) = \mathbf{M}_{jj} - \int_{-\Omega+\xi_j}^{\Omega+\xi_j} |G(\omega - \xi_j)|^2 S(\omega) d\omega = \int_{E_{\Omega, \xi_j}} |H_\alpha(\omega - \xi_j)|^2 S(\omega) d\omega, \quad (2.9)$$

where $E_{\Omega, \xi_j} = \mathbb{R} \setminus [-\Omega + \xi_j, \Omega + \xi_j]$, is precisely the aliasing-based bias in the estimator $\hat{S}(\xi_j)$. This error is of size

$$\mathbb{E}\varepsilon(\xi_j) = \int_{E_{\Omega, \xi_j}} \mathbb{E}|H_\alpha(\omega - \xi)|^2 S(\omega) d\omega \approx \|\boldsymbol{\alpha}\|_2^2 \int_{E_{\Omega, \xi_j}} S(\omega) d\omega,$$

where the expectation is taken over the random locations $\{x_j\}_{j=1}^n$. Thus we see that controlling the size of $\|\boldsymbol{\alpha}\|_2$ is critical to reducing this aliasing bias. To obtain a more precise concentration-type bound in terms of its relative size over the quantity to be estimated, $S(\xi)$, we provide the following theorem.

Theorem 2. *Let $S(\omega)$ be a valid spectral density, let points $\{x_j\}_{j=1}^n \stackrel{i.i.d.}{\sim} p(x)$, and let $\boldsymbol{\alpha} \in \mathbb{C}^n$ be corresponding weights to resolve the window function $g(x)$. Then under the assumptions listed above,*

$$P\{\varepsilon(\xi) \geq \beta S(\xi)\} \leq 2 \exp\left\{-\frac{\beta S(\xi)}{2 \|\boldsymbol{\alpha}\|_2^2 \int_{E_{\Omega, \xi}} S(\omega) d\omega}\right\}.$$

This theorem gives a probabilistic control over the size of the aliasing bias $\varepsilon(\xi)$ relatively to $S(\xi)$. In particular, the event $\{\varepsilon(\xi) \geq \beta S(\xi)\}$ occurring would mean that one should *not* expect the estimator $\hat{S}(\xi)$ to achieve $-\log_{10} \beta$ correct digits in the sense that $|\hat{S}(\xi) - S(\xi)|/S(\xi) < \beta$. It does not directly correspond to the event of achieving $-\log_{10} \beta$ digits, but if $\varepsilon(\xi) > S(\xi)$, for example, then there is no chance of achieving even one correct digit. With this in mind, this bound is best interpreted as one that is informative about disqualifying events in which a certain relative error is achieved.

Before proving this result, we require a technical lemma. For maximum generality, we state and prove the lemma without the simplifying reductions from (A4). The proof Lemma 1 is provided in Appendix B.

Lemma 1. *Let $\{x_j\}_{j=1}^n \stackrel{i.i.d.}{\sim} p$ with $p(x)$ satisfying (A2). Additionally, let $\boldsymbol{\alpha} = [\alpha_j]_{j=1}^n$ be weights with $\sum_{j=1}^n \alpha_j = G_0 \in \mathbb{R}$. Then by a standard abuse of notation*

$$H_\alpha(\omega) = \sum_{j=1}^n e^{2\pi i \omega x_j} \alpha_j \rightsquigarrow \mathcal{CN}\left\{\left[\begin{array}{c} G_0 \varphi(\omega) \\ 0 \end{array}\right], \boldsymbol{\Sigma}\right\},$$

where \mathcal{CN} denotes the complex-normal distribution, $\boldsymbol{\alpha} = \mathbf{a} + i\mathbf{b}$, $\langle \cdot, \cdot \rangle$ denotes the Euclidean inner product, and $\boldsymbol{\Sigma}$ has entries given by

$$\begin{aligned}\boldsymbol{\Sigma}_{11} &= \|\mathbf{a}\|_2^2 \left(\frac{1 + \varphi(2\omega)}{2} - \varphi(\omega)^2 \right) + \|\mathbf{b}\|_2^2 \frac{1 - \varphi(2\omega)}{2} \\ \boldsymbol{\Sigma}_{12} = \boldsymbol{\Sigma}_{21} &= \langle \mathbf{a}, \mathbf{b} \rangle (\varphi(2\omega) - \varphi(\omega)^2). \\ \boldsymbol{\Sigma}_{22} &= \|\mathbf{a}\|_2^2 \frac{1 - \varphi(2\omega)}{2} + \|\mathbf{b}\|_2^2 \left(\frac{1 + \varphi(2\omega)}{2} - \varphi(\omega)^2 \right).\end{aligned}$$

Additionally, as $\omega \rightarrow \infty$ as well, we have the simplified limiting MGF for $|H_\alpha(\omega)|^2$ given by

$$\mathbb{E}e^{t|H_\alpha(\omega)|^2} \xrightarrow{n,\omega} \frac{1}{1 - t \|\boldsymbol{\alpha}\|_2^2} \quad (2.10)$$

for t such that the right-hand side is finite.

Armed with this result, we now prove Theorem 2.

proof of Theorem 2. Letting $q(x)$ be a valid density on $E_{\Omega,\xi}$, Jensen's inequality gives that

$$\mathbb{E}e^{t\varepsilon(\xi)} \leq \int_{E_{\Omega,\xi}} \mathbb{E}e^{t\frac{S(\omega)}{q(\omega)}|H_\alpha(\omega-\xi)|^2} q(\omega) d\omega.$$

Since $S(\omega)$ is a spectral density, we note that $q(\omega) = CS(\omega)$ is a valid probability density for $C = \left(\int_{E_{\Omega,\xi}} S(\omega) d\omega \right)^{-1}$. Substituting this choice of q gives

$$\mathbb{E}e^{t\varepsilon(\xi)} \leq C \int_{E_{\Omega,\xi}} M_{|H_\alpha(\omega-\xi)|^2}(t/C) S(\omega) d\omega \approx \frac{C}{1 - \frac{t}{C} \|\boldsymbol{\alpha}\|_2^2} \int_{E_{\Omega,\xi}} S(\omega) d\omega = \frac{1}{1 - \frac{t}{C} \|\boldsymbol{\alpha}\|_2^2}.$$

With this bound on the MGF established, by a Chernoff bound with $t = \frac{\delta C}{\|\boldsymbol{\alpha}\|_2^2}$, $\delta \in [0, 1)$, we see that

$$P \{ \varepsilon(\xi) \geq \beta S(\xi) \} \leq \frac{\exp \{ -t\beta S(\xi) \}}{1 - \frac{t}{C} \|\boldsymbol{\alpha}\|_2^2} = (1 - \delta)^{-1} \exp \left\{ - \frac{\delta \beta S(\xi)}{\|\boldsymbol{\alpha}\|_2^2 \int_{E_{\Omega,\xi}} S(\omega) d\omega} \right\}.$$

Picking the specific case of $\delta = 1/2$ completes the proof. \square

Several consequences and interpretive conclusions follow from this theorem. First, we see that if $\|\boldsymbol{\alpha}\|_2$ were to blow up, the bound on aliasing errors would lose all power. As discussed in Sections 2.1 and 2.2, this blowup happens precisely when one either tries to resolve too high of a maximum frequency Ω or selects a poor window function $g(x)$. As Equation 2.1 and this theorem make clear, this aliasing error will pollute *every* estimate $\hat{S}(\xi)$, even if $\xi \ll \Omega$. So before computing any estimator, one must confirm that the weights $\boldsymbol{\alpha}$ are not only a high-accuracy solution to (2.3), but also are small in norm. Finally, we observe that the sampling scheme $p(x)$ (or equivalently $\varphi(\omega)$) does not directly impact this tail aliasing error in the sense that $\varphi(\omega)$ is asymptotically irrelevant to the distribution of $|H_\alpha(\omega)|^2$. It

is important to keep in mind, however, that the distribution of sampling locations plays a crucial role in the size of $\|\boldsymbol{\alpha}\|_2$ in practice, and thus should be considered when selecting a window function g .

Due to its significance in the study of Gaussian processes, we close with a corollary to Theorem 2 in the case of a Matérn process, for which the tail of $S(\omega)$ resembles a simple power law.

Corollary 2. *Given the setting of Theorem 2, consider the particular case of $S(\omega) \propto (\rho^2 + \omega^2)^{-\nu-1/2} \approx \omega^{-2\nu-1}$ for $\omega > M$, and assume that Ω , ξ , and $\Omega - \xi$ are all greater than M . Then the aliasing bias bounds simplify to*

$$P\{\varepsilon(\xi) \geq \beta S(\xi)\} \leq 2 \exp\left\{-\frac{2\nu\beta\xi^{-2\nu-1}}{(-\Omega + \xi)^{-2\nu} + (\Omega + \xi)^{-2\nu}}\right\}$$

Proof. Standard calculus and the assumed tail approximation give that

$$\int_{-\infty}^{-\Omega+\xi} S(\omega) d\omega \approx \frac{(-\Omega + \xi)^{-2\nu}}{2\nu}$$

Applying this result to the other segment in $E_{\Omega,\xi} = [-\infty, -\Omega + \xi] \cup [\Omega + \xi, \infty]$, simplifying, and condensing terms gives the final result. \square

A particularly clear circumstance and simplification of this bound comes in the case of $\xi > 0$ being near Ω in magnitude, so that $(-\Omega + \xi)^{-2\nu} + (\Omega + \xi)^{-2\nu} \approx (-\Omega + \xi)^{-2\nu}$ (indicating that the lower aliasing error from (2.1) dominates the upper aliasing error). In this setting, we can simplify the bound further to

$$2 \exp\left\{-\frac{2\nu\beta\xi^{-2\nu-1}}{(-\Omega + \xi)^{-2\nu} + (\Omega + \xi)^{-2\nu}}\right\} \approx 2 \exp\left\{-\frac{2\nu\beta}{\xi} \left(\frac{\xi}{\xi - \Omega}\right)^{-2\nu}\right\}.$$

As can be seen in this form, this bound is exceptionally weak for small ν , for example $\nu = \frac{1}{2}$ corresponding to the Ornstein-Uhlenbeck process, highlighting the difficulty of controlling aliasing error if one tries to be ambitious about resolving higher and higher frequencies ξ for such a process. We note that these simplifications assume sufficiently large ξ that the affect of ρ is negligible on $S(\xi)$, and so for processes with a large ρ these reductions will likely never be particularly accurate for achievable data sizes. But for more weakly dependent data, the approximation can be reasonably accurate for plausible data sizes.

3 Numerical demonstrations

To begin, we recall that $\mathbb{E}\hat{S}(\xi) = (|H_\alpha|^2 * S)(\xi)$ and provide a visual example of functions H_α and S which are convolved. Figure 4 shows a plot of an SDF $S(\omega)$ and the window function integrand $|H_\alpha(\omega - \xi)|^2$ computed for two different values of n with Ω fixed. As the plot illustrates, for fixed Ω and growing n , one can expect $\|\boldsymbol{\alpha}\|_2$ to decrease (shown in dotted horizontal lines). By the above theory, this will result in smaller aliasing biases for every estimate $\hat{S}(\omega)$. This visualization also provides some intuition about the relative sizes of the

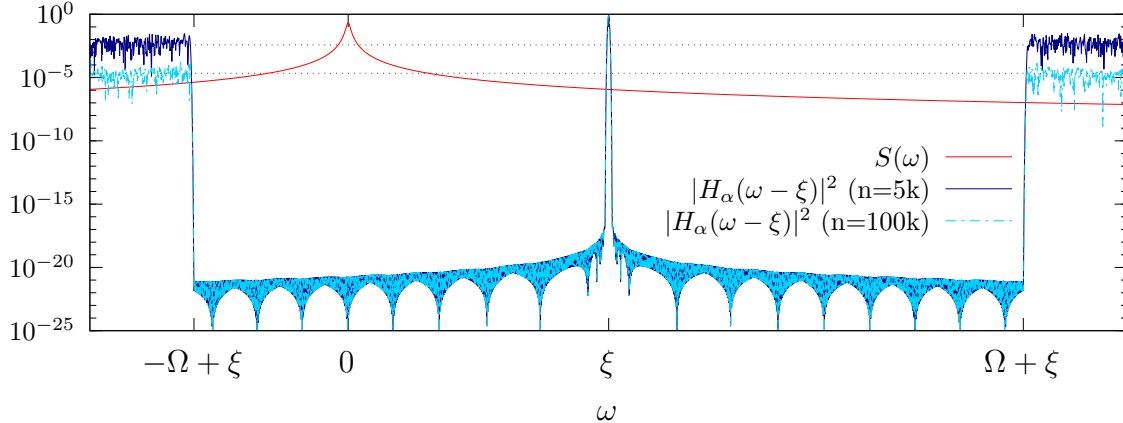


Figure 4: A visualization of the two terms in the integral of Equation 2.1, showing the behavior of $H_\alpha(\omega)$ outside of the resolved frequencies $[-\Omega, \Omega]$. Dotted lines give $\|\alpha\|_2^2$ for weights computed at two different n values.

aliasing terms. As ξ approaches Ω , for example, the lower aliasing term dominates the upper term, as the uncontrolled region of $|H_\alpha(\omega - \xi)|^2$ with $\omega < \xi - \Omega$ is multiplied with larger values of $S(\omega)$ than the corresponding “upper” aliasing term.

As a second demonstration of the role of $\|\alpha\|_2$ in controlling aliasing bias, we revisit the setting of Figure 3, this time picking sampling locations $\{x_j\}_{j=1}^n \stackrel{\text{i.i.d.}}{\sim} \text{Unif}([-1, 1] \setminus [-\tau, 0])$, simulating a Matérn process with spectral density $S(\omega) = C(\nu, \rho)\sigma^2(2\nu/\rho^2 + 4\pi^2\omega^2)^{-\nu-1/2}$ [43] and parameters $(\sigma, \rho, \nu) = (1, 0.1, 0.75)$, and attempting to estimate $S(\omega)$. This process exhibits strong dependence and slow spectral decay, and represents a setting where aliasing bias is a particularly serious concern. Figure 5 shows the result of choosing $g(x)$ to be either a standard Kaiser window supported on $[-1, 1]$ or a prolate function supported on the union of the two disjoint sampling intervals for several values of τ . As the figure demonstrates, for small enough τ the two estimators behave reasonably similarly, but as the gap τ increases and the norm $\|\alpha\|_2$ increases the estimates $\hat{S}(\xi)$ eventually are uniformly ruined by the size of the aliasing errors. We emphasize, however, that even with the moderate gap the Kaiser-based $G(\omega)$ is recovered reasonably well by the weights α as demonstrated in Figure 3. So the failure here is not that there is no α such that $\mathcal{F}\alpha \approx \mathbf{b}$, but rather that the α which provides the best approximate solution to that system has large norm.

Another way to understand which window functions $g(x)$ can be well-approximated using weights α with small norm is to more closely inspect the implications of Theorem 1. Figure 6 shows the absolute and relative maximum errors in window recovery of a Kaiser function with sampling schemes with and without a gap. From the left panel, we note that that in the case where the sampling regime has a gap we fail to recover an $H_\alpha(\omega)$ which approximates $G(\omega)$ well. However, the right panel illustrates that this failure is due to the limitations of finite-precision arithmetic and not the mathematical properties of $G(\omega)$. This further highlights the relevance of carefully selecting a window function $g(x)$ such that good *absolute* error is achieved, which is closely connected to the weights α having a favorably small norm.

Next, Figure 7 provides a visual investigation into the magnitude of aliasing error and a

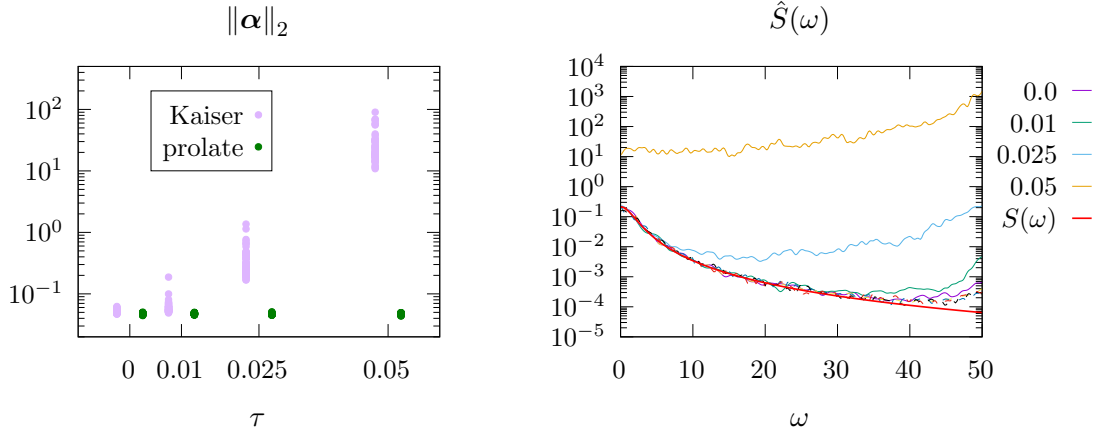


Figure 5: Expected values for spectral density estimators computed from $n = 1,000$ samples of a Matérn process given at uniform locations on the domain $[-1, 1] \setminus [-\tau, 0)$. Left panel: the norm of weights α with growing τ (x-axis) for $g(x)$ chosen to be a Kaiser on $[-1, 1]$ or a prolate on $[-1, 1] \setminus [-\tau, 0)$. Right panel: the expected \hat{S} in each case, with colors representing values of τ , solid lines giving the estimator using the Kaiser-computed α , and dotted lines using the prolate-computed α . The true spectral density $S(\omega)$ is shown in red. All weights are computed to resolve up to $\Omega = 50$.

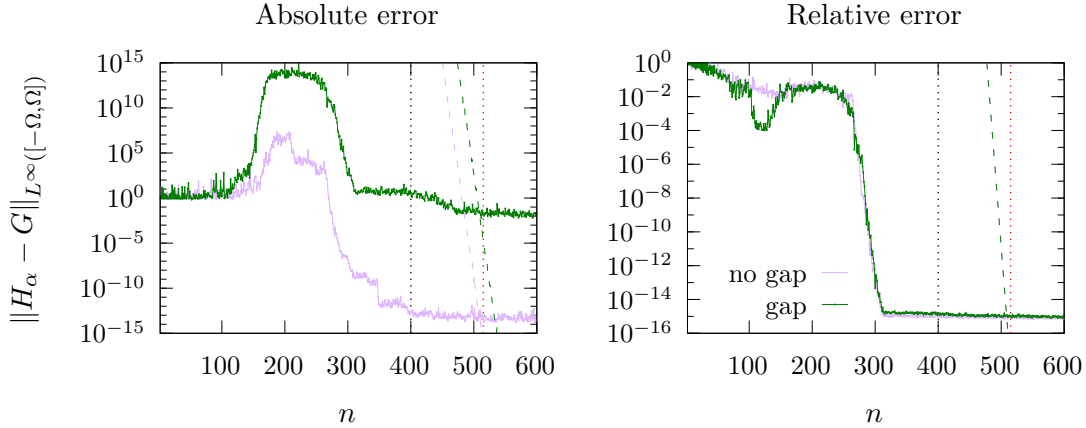


Figure 6: Maximum absolute error in Kaiser window recovery with n uniform points on $[-1, \tau] \cup [0, 1]$ for $\tau = 0$ (purple) and $\tau = 0.15$ (green) for a fixed $\Omega = 400$. The corresponding dotted lines show the exponentially decaying error bounds of Theorem 1 with $\rho = 3$. The dotted black line shows $n = 4\Omega(b - a)$ which corresponds to Nyquist sampling, and the dotted red line shows the bound given in Corollary 1.

validation of Theorem 2. For this study, we simulate $s = 100$ samples of $n = 5000$ uniform locations on $[-1, 1]$, and attempt to estimate $S(\xi)$ from samples of a Matérn process with parameters $(\sigma, \rho, \nu) = (1, 0.05, 0.5)$, representing an even more significant aliasing risk than above due to the slow spectral decay. Recalling that for random sampling locations $\varepsilon(\xi_j)$ is a random quantity, Figure 7 compares the empirical probability $\hat{P} \{ \varepsilon(\xi_j) \geq \beta S(\xi_j) \}$ with the

bounds provided by Theorem 2 for choices $\beta = 0.01$ (solid lines) and $\beta = 1$ (dotted lines). Several observations are immediately clear: first, we see that the bound of Theorem 2 is much sharper in quantifying high-probability events than low-probability events, and so in settings where one wishes to use this result to select the highest frequency to estimate, it would be more productive to do so by picking a β representing the highest level of precision one is willing to *lose*, and finding the frequency for which the theoretical bound hits one.

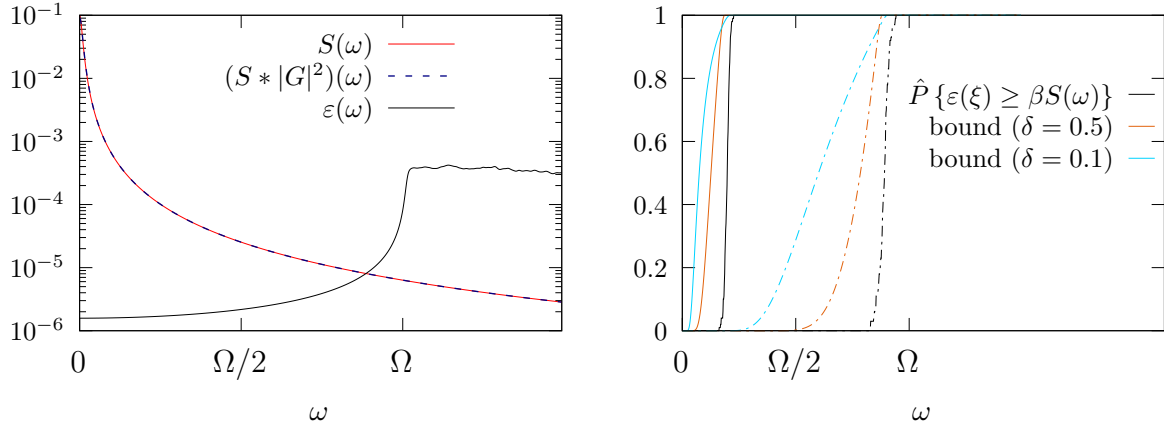


Figure 7: An empirical investigation comparing true aliasing biases (computed using (2.9)) with the theoretical bound given in Theorem 2. In the right panel, solid lines are for $\beta = 0.01$, and dotted are for $\beta = 1$, and the blue line demonstrates the bound computed with $\delta = 0.1$ instead of $\delta = 0.5$ in the final line of the proof of Theorem 2.

Moving to two dimensions, we now consider an analogous problem of estimating the spectral density $S(\boldsymbol{\omega})$ for a process $Y(\boldsymbol{x})$ defined on $[0, 1]^2$. Conceptually, the framework for this estimation problem is exactly the same: obtain a window function $g(\boldsymbol{x})$ for which its Fourier transform $G(\boldsymbol{\omega})$ gives a right-hand side $\mathbf{b} = [G(\boldsymbol{\omega}_k)]_{k=1}^n$ whose corresponding $\boldsymbol{\alpha}$ lives in the linear span of the non-degenerate singular vectors of \mathcal{F} , whose entries are simply extended to be defined as $\mathcal{F}_{jk} = e^{-2\pi i \boldsymbol{\omega}_k^T \boldsymbol{x}_j}$. In Figure 8 we provide a demonstration that this framework still provides a productive way forward and accurate estimator. In particular, in Figure 8 we draw $\{\boldsymbol{x}_j\}_{j=1}^n \stackrel{\text{i.i.d.}}{\sim} \text{Unif}([-1, 1]^2)$ for $n = 65,000$, and sample a highly anisotropic Matérn process at those points. We then use the above procedure to obtain weights $\boldsymbol{\alpha}$ and compute the SDF estimator $\hat{S}(\boldsymbol{\xi}) = \left| \sum_{j=1}^n e^{-2\pi i \boldsymbol{x}_j^T \boldsymbol{\xi}} \alpha_j y_j \right|^2$, just as in the univariate case. The window function $g(\boldsymbol{x})$ used in Figure 8 is a prolate function whose Fourier transform $G(\boldsymbol{\omega})$ is concentrated on a ball of radius 2 around the origin, which in the language of Equation 2.7 corresponds to selecting $\mathcal{R} = \{\boldsymbol{\omega} : \|\boldsymbol{\omega}\|_2 < 2\}$. For details on computing $\boldsymbol{\alpha}$ and prolate functions in general quickly and accurately, we refer the reader to Appendix A.

Several comments about this estimator are in order. First, we see that, unlike in the one-dimensional case, the convolution $S * |G|^2$ does introduce a notable blurring of the features of S , and so local bias due to the window function in this higher dimensional setting is a much more significant concern than in one dimension (consider for contrast the left panel of Figure 7, which shows that in one dimension $S(\xi) \approx (S * |G|^2)(\xi)$ to high accuracy). As a second point, readers will note that the marginal frequencies ξ_1 and ξ_2 for which $S(\boldsymbol{\xi})$ is being

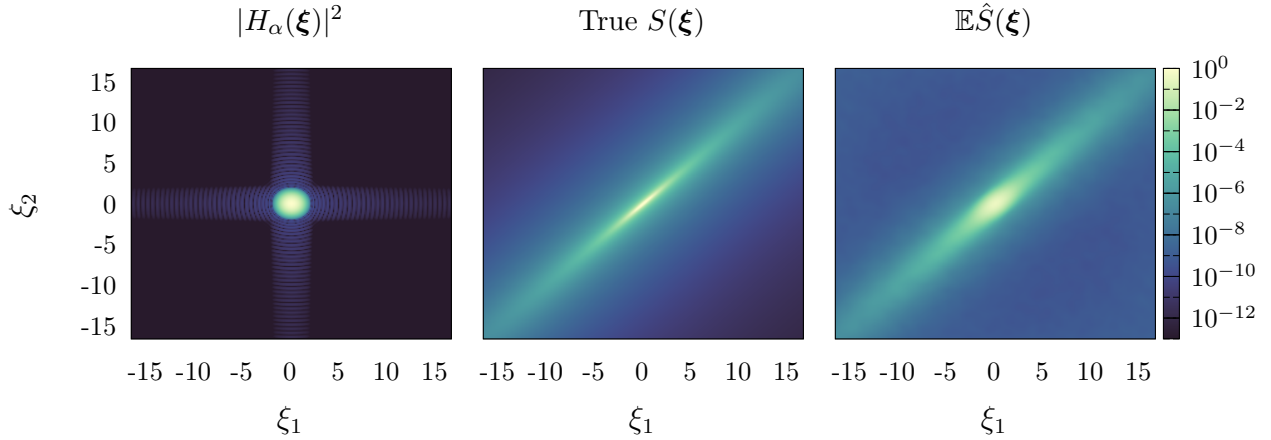


Figure 8: A two-dimensional nonparametric spectral density estimator for $n = 65,000$ samples from an anisotropic Matérn process on $[0, 1]^2$, with the last panel giving a Monte Carlo approximation to the expectation.

estimated are quite small, even for $n = 65,000$ points on a relatively small domain. This is because the highest resolvable frequency will grow in norm with $n^{1/d}$ in d dimensions. So even with a very large dataset on a lattice over $[-1, 1]^2$, for example with $n = 100,000$, the marginal slices in each dimension will be of length $\sqrt{n} \approx 316$, and by information-theoretic limits as discussed above one cannot (nonparametrically) estimate spectral densities at high frequencies with so few points. Finally, we note that the essence of Theorem 2 applies just as directly in this setting with the modification that $E_{\Omega, \xi} = \mathbb{R}^2 \setminus [-\Omega, \Omega]^2$. As such, it will likely often be the case that the aliasing error will be significantly harder to control in multiple dimensions. Given the above intuition about how slowly one resolves higher frequencies in each marginal single dimension, this is not surprising.

4 Discussion

In this work, we present a framework for nonparametric spectral density estimation that applies to fully irregularly sampled measurements in one or more dimensions. The key insight is to implicitly obtain quadrature weights such that the variance of the weighted nonuniform Fourier sums can be interpreted as integral transforms of the SDF in a way that mimics the standard univariate gridded setting. This estimator demonstrates significant practical improvement over periodogram or Lomb-Scargle least squares-based approaches. However, there are also limitations to its accuracy due to aliasing-based sources of bias in the tails of the spectral density, and there is a direct tradeoff between how far in the tails of an SDF one hopes to estimate and the chance of aliasing biases dominating the variance of the true signal one is attempting to observe.

This work motivates many new and important questions. Perhaps most importantly, if one wishes to estimate the SDF at or near the highest resolvable frequency, the runtime cost of computing α with the methods we discuss here is $\mathcal{O}(n^3)$. Considering that the action of \mathcal{F} on a vector can be computed rapidly using the NUFFT, it is natural to ask if this can be

improved. In most fixed-domain asymptotic sampling regimes, we expect \mathcal{F} to be sufficiently poorly conditioned that it is not of full numerical rank, making existing fast methods for solving least-squares problems not directly applicable [25, 26, 53]. Due to this ill-conditioning, implicit Krylov-type methods that can be done with only matrix-vector products often do not converge. With that said, many of the numerical methods needed to obtain weights α in $\mathcal{O}(n \log n)$ time exist, and so we are hopeful that it is possible to devise an algorithm to compute these weights quickly and achieve parity with the excellent runtime scaling of gridded nonparametric SDF estimators. Importantly, this problem is strictly easier than the general problem of nonuniform Fourier inversion—we have the ability to choose the window $g(x)$ so that the corresponding right-hand side $\mathbf{b} = [G(\omega_k)]_{k=1}^n$ to the linear system lies in the span of the dominant singular vectors of the poorly conditioned nonuniform Fourier matrix \mathcal{F} . Similarly, in the case of gappy regular data we note that the above method reduces to something very similar to the method described in [8, 21]. In such a case where \mathcal{F} is well-conditioned, any standard fast least squares method would perform well, and using NUFFTs [11, 4] would make the computation of weights α possible in $\mathcal{O}(n \log n)$.

Secondly, the theory and practice of window design in this setting has not been explored fully. While prolate functions can be computed in $\mathcal{O}(n \log n)$ (see Appendix A) and are certainly not the bottleneck in obtaining weights α , this work leaves several open questions about when a window function g is a “good” window function for a given set of points. One simple adaptive approach is to choose a window $g(x)$ which spans the entire domain of data collection, compute weights α , and, if their norm is large, subdivide the domain across the largest gap or by clustering, and compute a prolate window on the union of the two disjoint domains. This process can be continued recursively until $\|\alpha\|_2$ is sufficiently small. The heuristic SVD-based argument in Section 2.2 may also be made precise by considering a continuous SVD [46] of the system of complex exponentials $\{e^{-2\pi i \omega x_j}\}_{j=1}^n$ and forming a maximally-concentrated $G(\omega)$ explicitly as a linear combination of its dominant singular functions. This and related questions are exciting avenues of future work.

Acknowledgments

The authors would like to thank Rishabh Dudeja for suggesting the Jensen inequality mechanism used in the proof of Theorem 2, and Michael O’Neil for helpful conversations throughout the development process.

Competing Interests

The authors report no competing interests.

References

- [1] B. Adcock, M. Gataric, and A. Hansen. On stable reconstructions from nonuniform Fourier measurements. *SIAM Journal on Imaging Sciences*, 7(3):1690–1723, 2014.
- [2] A. Aldroubi and K. Gröchenig. Nonuniform sampling and reconstruction in shift-invariant spaces. *SIAM review*, 43(4):585–620, 2001.

- [3] P. Babu and P. Stoica. Spectral analysis of nonuniformly sampled data—a review. *Digital Signal Processing*, 20(2):359–378, 2010.
- [4] A.H. Barnett, J. Magland, and L. af Klinteberg. A parallel nonuniform fast Fourier transform library based on an “exponential of semicircle” kernel. *SIAM Journal on Scientific Computing*, 41(5):C479–C504, 2019.
- [5] J.J. Benedetto. Irregular sampling and frames. *wavelets: A Tutorial in Theory and Applications*, 2:445–507, 1992.
- [6] P.J. Brockwell. *Time series: Theory and methods*. Springer-Verlag, 1991.
- [7] T.P. Bronez. Spectral estimation of irregularly sampled multidimensional processes by generalized prolate spheroidal sequences. *IEEE Transactions on Acoustics, Speech, and Signal Processing*, 36(12):1862–1873, 1988.
- [8] A.D. Chave. A multitaper spectral estimator for time-series with missing data. *Geophysical Journal International*, 218(3):2165–2178, 2019.
- [9] J. Cui, B.H. Brinkmann, and G.A. Worrell. A fast multitaper power spectrum estimation in nonuniformly sampled time series. *arXiv preprint arXiv:2407.01943*, 2024.
- [10] S. Dodson-Robinson and C. Haley. Optimal frequency-domain analysis for spacecraft time series: Introducing the missing-data multitaper power spectrum estimator. *The Astronomical Journal*, 167(1):22, 2023.
- [11] A. Dutt and V. Rokhlin. Fast Fourier transforms for nonequispaced data. *SIAM Journal on Scientific computing*, 14(6):1368–1393, 1993.
- [12] A. Glaser, X. Liu, and V. Rokhlin. A fast algorithm for the calculation of the roots of special functions. *SIAM Journal on Scientific Computing*, 29(4):1420–1438, 2007.
- [13] G.H. Golub and J.H. Welsch. Calculation of Gauss quadrature rules. *Mathematics of computation*, 23(106):221–230, 1969.
- [14] L. Greengard, J.Y. Lee, and S. Inati. The fast sinc transform and image reconstruction from nonuniform samples in k-space. *Communications in Applied Mathematics and Computational Science*, 1(1):121–131, 2007.
- [15] P. Greengard. Generalized prolate spheroidal functions: algorithms and analysis. *Pure and Applied Analysis*, 6(3):789–833, 2024.
- [16] K. Gröchenig. A discrete theory of irregular sampling. *Linear Algebra and its applications*, 193:129–150, 1993.
- [17] K. Gröchenig. *Foundations of time-frequency analysis*. Springer Science & Business Media, 2001.

- [18] D.M. Gruenbacher and D.R. Hummels. A simple algorithm for generating discrete prolate spheroidal sequences. *IEEE Transactions on signal processing*, 42(11):3276–3278, 2002.
- [19] M. Gu and S.C. Eisenstat. Efficient algorithms for computing a strong rank-revealing QR factorization. *SIAM Journal on Scientific Computing*, 17(4):848–869, 1996.
- [20] N. Hale and A. Townsend. Fast and accurate computation of Gauss–Legendre and Gauss–Jacobi quadrature nodes and weights. *SIAM Journal on Scientific Computing*, 35(2):A652–A674, 2013.
- [21] C.L. Haley. Missing-data multitaper coherence estimation. *IEEE Signal Processing Letters*, 28:1704–1708, 2021.
- [22] N. Halko, P.G. Martinsson, and J.A. Tropp. Finding structure with randomness: Probabilistic algorithms for constructing approximate matrix decompositions. *SIAM review*, 53(2):217–288, 2011.
- [23] J. Kaiser and R. Schafer. On the use of the I_0 -sinh window for spectrum analysis. *IEEE Transactions on Acoustics, Speech, and Signal Processing*, 28(1):105–107, 1980.
- [24] A. Khintchine. Korrelationstheorie der stationären stochastischen Prozesse. *Mathematische Annalen*, 109(1):604–615, 1934.
- [25] M. Kircheis and D. Potts. Direct inversion of the nonequispaced fast Fourier transform. *Linear Algebra and its Applications*, 575:106–140, 2019.
- [26] M. Kircheis and D. Potts. Fast and direct inversion methods for the multivariate nonequispaced fast Fourier transform. *Frontiers in Applied Mathematics and Statistics*, 9:1155484, 2023.
- [27] N. Kovvali. *Theory and applications of Gaussian quadrature methods*. Springer Nature, 2022.
- [28] HJ Landau. Sampling, data transmission, and the Nyquist rate. *Proceedings of the IEEE*, 55(10):1701–1706, 1967.
- [29] N.R. Lomb. Least-squares frequency analysis of unequally spaced data. *Astrophysics and space science*, 39:447–462, 1976.
- [30] F.W.J. Olver. *NIST handbook of mathematical functions hardback and CD-ROM*. Cambridge university press, 2010.
- [31] S.J. Orfanidis. *Introduction to signal processing*. Prentice-Hall, Inc., 1995.
- [32] V.Y. Pan. How bad are Vandermonde matrices? *SIAM Journal on Matrix Analysis and Applications*, 37(2):676–694, 2016.

- [33] A.A. Patil, G.M. Eadie, J.S. Speagle, and D.J. Thomson. Improving harmonic analysis using multitapering: Precise frequency estimation of stellar oscillations using the harmonic f-test. *arXiv preprint arXiv:2405.18509*, 2024.
- [34] D.B. Percival and A.T. Walden. *Spectral analysis for univariate time series*, volume 51. Cambridge University Press, 2020.
- [35] G.A. Prieto, R.L. Parker, D.J. Thomson, F.L. Vernon, and R.L. Graham. Reducing the bias of multitaper spectrum estimates. *Geophysical Journal International*, 171(3):1269–1281, 2007.
- [36] K.S. Riedel and A. Sidorenko. Minimum bias multiple taper spectral estimation. *IEEE Transactions on Signal Processing*, 43(1):188–195, 1995.
- [37] J.D. Scargle. Studies in astronomical time series analysis. II. Statistical aspects of spectral analysis of unevenly spaced data. *Astrophysical Journal, Part 1, vol. 263, Dec. 15, 1982, p. 835-853.*, 263:835–853, 1982.
- [38] C.E. Shannon. Communication in the presence of noise. *Proceedings of the IRE*, 37(1):10–21, 1949.
- [39] F.J. Simons and D.V. Wang. Spatiospectral concentration in the Cartesian plane. *GEM-International Journal on Geomathematics*, 2:1–36, 2011.
- [40] D. Slepian. Some comments on fourier analysis, uncertainty and modeling. *SIAM review*, 25(3):379–393, 1983.
- [41] D. Slepian and H.O. Pollak. Prolate spheroidal wave functions, Fourier analysis and uncertainty—i. *Bell System Technical Journal*, 40(1):43–63, 1961.
- [42] A. Springford, G.M. Eadie, and D.J. Thomson. Improving the Lomb–Scargle periodogram with the thomson multitaper. *The Astronomical Journal*, 159(5):205, 2020.
- [43] M.L. Stein. *Interpolation of spatial data: some theory for Kriging*. Springer Science & Business Media, 1999.
- [44] P. Stoica and P. Babu. Maximum-likelihood nonparametric estimation of smooth spectra from irregularly sampled data. *IEEE Transactions on Signal Processing*, 59(12):5746–5758, 2011.
- [45] D.J. Thomson. Spectrum estimation and harmonic analysis. *Proceedings of the IEEE*, 70(9):1055–1096, 1982.
- [46] A. Townsend and L.N. Trefethen. Continuous analogues of matrix factorizations. *Proceedings of the Royal Society A: Mathematical, Physical and Engineering Sciences*, 471(2173):20140585, 2015.
- [47] Lloyd N Trefethen. *Approximation theory and approximation practice*. SIAM, 2019.
- [48] L.N. Trefethen and D. Bau. *Numerical linear algebra*. SIAM, 2022.

- [49] L.N. Trefethen and J.A.C. Weideman. The exponentially convergent trapezoidal rule. *SIAM review*, 56(3):385–458, 2014.
- [50] A.W. Van der Vaart. *Asymptotic statistics*, volume 3. Cambridge university press, 2000.
- [51] J.T. VanderPlas. Understanding the Lomb–Scargle periodogram. *The Astrophysical Journal Supplement Series*, 236(1):16, 2018.
- [52] A. Viswanathan, A. Gelb, D. Cochran, and R. Renaut. On reconstruction from non-uniform spectral data. *Journal of Scientific Computing*, 45:487–513, 2010.
- [53] H. Wilber, E.N. Epperly, and A.H. Barnett. Superfast direct inversion of the nonuniform discrete Fourier transform via hierarchically semi-separable least squares. *arXiv preprint arXiv:2404.13223*, 2024.
- [54] H. Xiao, V. Rokhlin, and N. Yarvin. Prolate spheroidal wavefunctions, quadrature and interpolation. *Inverse problems*, 17(4):805, 2001.
- [55] N. Yarvin and V. Rokhlin. Generalized Gaussian quadratures and singular value decompositions of integral operators. *SIAM Journal on Scientific Computing*, 20(2):699–718, 1998.

A Fast computation of prolate right-hand sides

This appendix will provide a terse set of instructions for obtaining and evaluating the Fourier transform of prolate functions in arbitrary dimensions on an arbitrary spatial domain \mathcal{D} that are concentrated on an arbitrary region \mathcal{R} in spectral space. The mathematical background and specific formulation of the problem discussed in this work is closest to the formulation given in [39], but unlike in that work we will discuss the application of fast algorithms to accelerate the computation of these functions. The end result of this set of instructions is the right-hand side $\mathbf{b} = [G(\boldsymbol{\omega}_k)]_{k=1}^n$, where $\{\boldsymbol{\omega}_k\}_{k=1}^n$ are the frequencies used in setting up the linear system (2.3).

1. First, we compute a quadrature rule with nodes $\{\mathbf{x}_j\}_{j=1}^L$ and weights $\{\gamma_j\}_{j=1}^L$ such that

$$\int_{\mathcal{D}} f(\mathbf{x}) \, d\mathbf{x} \approx \sum_{j=1}^L f(\mathbf{x}_j) \gamma_j$$

for smooth functions $f : \mathcal{D} \rightarrow \mathbb{R}$. For domains \mathcal{D} that are rectangles, a particularly simple strategy is to use a tensor product of univariate Gauss-Legendre rules. In more complex domains, obtaining such a rule may be quite complicated, and so this requirement is a potential limitation of this approach.

2. Armed with this quadrature rule, we now need to obtain the dominant eigenvector of the matrix corresponding to the discretized integral equation. Equation 2.7 can be discretized using the above quadrature rule to the linear system

$$\mathbf{T} \cdot \text{Diag}(\boldsymbol{\gamma}) \cdot \mathbf{g} = \lambda \mathbf{g}, \quad \mathbf{T}_{jk} = \int_{\mathcal{R}} e^{-2\pi i \boldsymbol{\omega}^T (\mathbf{x}_j - \mathbf{x}_k)} \, d\boldsymbol{\omega}.$$

In the one-dimensional case where $\mathbb{R} = [-W, W]$, for example, $\mathbf{T}_{jk} = \text{sinc}(W(x_j - x_k))$ (with slight variations based on how Fourier transforms and sinc are defined), and in two dimensions where \mathbb{R} is a ball of radius W , $\mathbf{T}_{jk} \propto (W \|\mathbf{x}_j - \mathbf{x}_k\|_2)^{-1} J_1(W \|\mathbf{x}_j - \mathbf{x}_k\|_2)$, the so-called “jinc” function.

The simplest option is to form the dense matrix $\mathbf{T} \cdot \text{Diag}(\boldsymbol{\gamma})$ and compute its full eigendecomposition to obtain the dominant eigenvector \mathbf{g} , which is the most concentrated prolate function. As an aside, there are often several well-concentrated eigenfunctions, which is the fundamental motivation of *multitaper* methods [45]. This computation is exceptionally expensive, scaling like $\mathcal{O}(L^3)$ with a significant prefactor due to being a non-symmetric eigenvalue problem. But at least in certain cases, the action of \mathbf{T} on a vector can be accelerated using an algorithm like the fast sinc transform [14], although in higher dimensions for different choices of \mathcal{R} the algorithm will require modification or specialization. Once such an algorithm has been implemented, the matrix-vector product implicitly represented with $\mathbf{t} \mapsto \mathbf{T} \cdot \text{Diag}(\boldsymbol{\gamma}) \cdot \mathbf{t}$ can be computed in $\mathcal{O}(L \cdot \text{polylog}L)$, and this implicit operator can be provided to a Krylov subspace routine library (many of which are available as libre software) to obtain the dominant eigenvector \mathbf{g} . One could take an adaptive approach to this integral discretization by choosing a small L and re-computing \mathbf{g} for increasing L and checking for self-convergence.

Alternatively, considering that prolate functions are very smooth, it is very likely that choosing L to resolve the oscillations in the computed entries of \mathbf{b} (see the next step for details) is more than enough to resolve \mathbf{g} .

3. If one has selected L large enough that the quadrature rule can resolve the highest-frequency oscillator $e^{-2\pi i \boldsymbol{\omega}_{\max}^T \mathbf{x}}$ on \mathcal{D} , one now simply computes the nonuniform Fourier transform using the same quadrature rule:

$$\mathbf{b}_k = \sum_{j=1}^L e^{-2\pi i \mathbf{x}_j^T \boldsymbol{\omega}_k} \mathbf{g}_j \gamma_j.$$

This computation can be accelerated with an NUFFT [11, 4], and so in the case where the action of \mathbf{T} has been accelerated with a fast analysis-based transform like the fast sinc transform the entire process of obtaining \mathbf{b} can be done in $\mathcal{O}(L \cdot \text{polylog}L)$ time. This was precisely how the prolate-based right-hand sides \mathbf{b} were obtained in this work, and their computation is much faster than the next step of obtaining weights $\boldsymbol{\alpha}$ by solving the least-squares problem (2.3).

If one has selected L to be smaller than the required number for resolving the highest oscillator in \mathbf{b} , then before such computation one must obtain a new quadrature rule of order L' that *can* resolve all the oscillations and then interpolate the obtained values $\{g(\mathbf{x}_j)\}$ to the nodes of the finer quadrature rule. From there, the same summation formula as above can be used to obtain \mathbf{b} .

B Proof of Lemma 1

Proof of Lemma 1. First, we break $H_\alpha(\omega)$ into its real and imaginary parts

$$\begin{aligned} H_\alpha^r(\omega) &= \sum_{j=1}^n \cos(2\pi\omega x_j) a_j - \sin(2\pi\omega x_j) b_j \\ H_\alpha^i(\omega) &= \sum_{j=1}^n \sin(2\pi\omega x_j) a_j + \cos(2\pi\omega x_j) b_j. \end{aligned}$$

For the first moments, we simply note that $\varphi(\omega)$ is real-valued by (A2) and we have that $\mathbb{E}H_\alpha^r(\omega) = G_0\varphi(\omega)$ and $\mathbb{E}H_\alpha^i(\omega) = 0$. For the second moments, the fundamental computations required are $\mathbb{V} \cos(2\pi\omega x_j)$, $\mathbb{V} \sin(2\pi\omega x_j)$, and $\text{Cov}(\cos(2\pi\omega x_j), \sin(2\pi\omega x_j))$. In all cases, these may be expressed using standard product-to-sum trigonometric formulae. As an example, we note that

$$\begin{aligned} \mathbb{V} \cos(2\pi\omega x_j) &= \mathbb{E} \cos(2\pi\omega x_j)^2 - (\mathbb{E} \cos(2\pi\omega x_j))^2 \\ &= \mathbb{E} \left\{ \frac{1}{2} [1 + \cos(2\pi(2\omega)x_j)] \right\} - \varphi(\omega)^2 \\ &= \frac{1}{2}(1 + \varphi(2\omega)) - \varphi(\omega)^2. \end{aligned}$$

By similar arguments, we see that $\mathbb{V} \sin(2\pi\omega x_j) = \frac{1}{2}(1 - \varphi(2\omega))$ and that the covariance of the cross term is $\text{Cov}(\cos(2\pi\omega x_j), \sin(2\pi\omega x_j)) = 0$. With this established, we first compute the marginal variance of $H_\alpha^r(\omega)$ as

$$\begin{aligned} \mathbb{V}H_\alpha^r(\omega) &= \mathbb{V} \left\{ \sum_{j=1}^n \cos(2\pi\omega x_j) a_j \right\} + \mathbb{V} \left\{ \sum_{j=1}^n \sin(2\pi\omega x_j) b_j \right\} \\ &= \|\mathbf{a}\|_2^2 \left(\frac{1 + \varphi(2\omega)}{2} - \varphi(\omega)^2 \right) + \|\mathbf{b}\|_2^2 \frac{1 - \varphi(2\omega)}{2} \end{aligned}$$

where the cross term is zero by above and the independence of the $\{x_j\}$ is used to bring the variance inside the sums. Similarly, we have that the marginal variance for $H_\alpha^i(\omega)$ is given as

$$\mathbb{V}H_\alpha^i(\omega) = \|\mathbf{a}\|_2^2 \frac{1 - \varphi(2\omega)}{2} + \|\mathbf{b}\|_2^2 \left(\frac{1 + \varphi(2\omega)}{2} - \varphi(\omega)^2 \right).$$

Finally, by similar or straightforward definitional computations, we see that

$$\text{Cov}(H_\alpha^r(\omega), H_\alpha^i(\omega)) = \langle \mathbf{a}, \mathbf{b} \rangle (\varphi(2\omega) - \varphi(\omega)^2).$$

With the first and second moments computed, the first claim follows from the Lyapunov central limit theorem.

For the second claim, we note that for each ω and n , $|H_\alpha(\omega)| \leq \|\boldsymbol{\alpha}\|_1 = \mathcal{O}(1)$ by (A5), so that the doubly-indexed collection of random variables is uniformly bounded and thus asymptotically uniformly integrable, and the same is true for the family of random variables $e^{t|H_\alpha(\omega)|^2}$. By standard results on uniform integrability (for example [50, Theorem 2.20]), we have that $e^{t|H_\alpha(\omega)|^2}$ converges in expectation as well as in law. For a random variable $\mathbf{s} \sim \mathcal{N}\{\mathbf{0}, \mathbf{C}\}$, the moment generating function of $\mathbf{s}^T \mathbf{s}$ is given by

$$\mathbb{E} e^{t\mathbf{s}^T \mathbf{s}} = |\mathbf{I} - 2t\mathbf{C}|^{-1/2}, \tag{B.1}$$

and applying in this case to the asymptotic variance $\mathbf{C} = \boldsymbol{\Sigma}$ with $\omega \rightarrow 0$ reduces \mathbf{C} to $\|\boldsymbol{\alpha}\|_2^2 \mathbf{I}$. Plugging this reduction in (B.1) gives the desired result. \square